Quantifying ultrafast energy transfer from plasmonic hot carriers for pulsed photocatalysis on nanostructures

Andrea Schirato[# 1,2,3], Stephen Sanders[# 2], Remo Proietti Zaccaria[3,4], Peter Nordlander[2,5], Giuseppe Della Valle[1,6], Alessandro Alabastri[* 2]

*e-mail address: alessandro.alabastri@rice.edu
[#] A.S. and S.S. equally contributed to this work

[1] Department of Physics, Politecnico di Milano, 20133 Milano, Italy
[2] Department of Electrical and Computer Engineering, Rice University, Houston, Texas 77005, United States
[3] Istituto Italiano di Tecnologia, 16163 Genoa, Italy
[4] Cixi Institute of Biomedical Engineering, Ningbo Institute of Industrial Technology, Chinese Academy of Sciences, 1219 Zhongguan West Road, Ningbo 315201, China
[5] Department of Physics and Astronomy, Laboratory for Nanophotonics, Rice University, 6100 Main Street, Houston, TX 77005
[6] Istituto di Fotonica e Nanotecnologie - Consiglio Nazionale delle Ricerche, Piazza Leonardo da Vinci, 32, I-20133 Milano, Italy

Keywords: photocatalysis, ultrafast nanophotonics, hot carriers, photothermal

Abstract

Photocatalysis with plasmonic nanostructures has lately emerged as a new, transformative paradigm to drive and alter chemical reactions using light. At the surface of metallic nanoparticles, photoexcitation results in strong near fields, short-lived high-energy 'hot' carriers, and light-induced heating, thus creating a unique local environment where reactions can occur with enhanced efficiencies. In this context, it is critical to understand and how to manipulate the nonequilibrium processes triggered by light, as their ultrafast (femto- to picoseconds) relaxation dynamics compete with the process of energy transfer towards the reactants. Accurate predictions of the plasmon photocatalytic activity can lead to optimized nanophotonic architectures with enhanced selectivity and rates, operating beyond the intrinsic limitations of the steady state. Here, we report on an original modeling approach to quantify, with space, time, and energy resolution, the ultrafast energy exchange from plasmonic hot carriers to molecular systems adsorbed on the metal nanoparticle surface while consistently accounting for photothermal bond activation.

Our analysis, illustrated for a few typical cases, reveals that the nonthermal fraction of carriers (i.e., with the highest excess energies) may introduce a wavelength-dependence of the reaction rates and sheds light on the role of nonequilibrium thermal carriers (i.e., those closer to the Fermi level), in particular regarding the photothermally heated lattice, suggesting ways to enhance and optimize each contribution. We show that the overall reaction rates can benefit strongly from using pulsed illumination with the optimal pulse width determined by the properties of the system. Taken together, these results pave the way for the rational design of nanoreactors for pulsed catalysis, leveraging predictive modeling of the ultrafast hot carrier-hot adsorbate energy transfer.

Introduction

The use of light and nanoparticles (NPs) to drive chemical reactions has recently gained increasing attention as an innovative, sustainable solution for the chemical industry. This sector, typically fed by fossil fuels, represents one of the largest energy consumers globally (~2.5% of the world's usage), with annual greenhouse gas emissions near the gigaton level (~1.5% of global values)[1, 2]. Incident photons on these metallic nanostructures can excite electron-hole pairs and promote peculiar optical phenomena to create a unique local environment where reactions can proceed by light[3-6]. In particular, the resonant photoexcitation of plasmonic NPs produces a coherent oscillation of charges, known as Localised Surface Plasmon (LSP), which confines electromagnetic fields in nanometric volumes[7, 8]. Upon dephasing, the LSP decays by generating charge excitations, i.e., high-energy 'hot' carriers (HCs)[9, 10], that can interact with nearby reactants while in their nonequilibrium state via the injection into an unoccupied molecular orbital[11-14]. Through subsequent electron-electron and electron-phonon scattering, HCs equilibrate with the lattice, dissipating heat and locally increasing the temperature[15, 16]. By leveraging synergistically these light-induced effects, plasmonic photothermal catalysis has opened unprecedented opportunities for studying and controlling chemical reactions in optical systems[17, 18]. To date, several experimental demonstrations have been reported, indicating the possibility of, e.g., driving unfavorable reactions at low temperatures and pressures, modifying reactivities, or unlocking reaction pathways otherwise inaccessible[19-26].

In this framework, understanding the interaction mechanisms between light, charge carriers, and phonons in the metal and the molecules adsorbed at the NP surface is of paramount importance. A systematic, quantitative description of these phenomena could contribute to developing optimized nanophotonic platforms and identify the design principles for enhanced-performance nano-reactors. The task, however, requires accounting for a variety of interdependent events taking place on mismatched length, energy, and time scales. This is especially true for the HC component, which is concurrently the most intriguing (it leads to unique phenomena, e.g., changes in energy barriers for specific reactions[27-31]) and the most challenging to control, mainly due to the short lifetimes of the carriers[32]. Once photogenerated, HCs undergo ultrafast relaxation processes, returning them to equilibrium within a characteristic time ranging from hundreds of femtoseconds to a few picoseconds[33, 34]. During these ultrafast timescales, the HC relaxation competes with the injection and energy transfer to the adsorbate[35-37]. It is therefore essential to gain insight into the dynamical interactions of HCs and chemical species at the surface of plasmonic NPs.

Importantly, investigating photocatalytic events in the time domain is not only of fundamental interest. Recent studies have reported significant advantages in terms of chemical reactivity when working in the pulsed regime over the steady state, i.e., under continuous-wave (CW) illumination.
Changes in the rate-limiting steps of a reaction upon periodic illumination[38] and modified sub-ps HC dynamics in the presence of adsorbates[39] have been experimentally demonstrated. In addition, numerical predictions have revealed that inducing photothermal heating of plasmonic NPs via ultrafast light pulses matching the timescale of elementary reaction steps (ps to ns) can lead to a favorable, dynamic mode of operation with higher energy efficiency and catalyst activity[40-42], along the same lines of a few theoretical studies of chemical activity under thermal modulation[43, 44]. These intriguing results, together with the great promise of using solid-state lighting sources such as lasers and LEDs to excite photocatalytic nanostructures[27], bring the ultrafast regime of plasmonic photocatalysis to the spotlight and call for a comprehensive modeling approach to interpret and gauge the HC- and temperature-driven photocatalytic processes at the NP surface in the time domain.

To date, several theoretical studies have focussed, primarily via accurate first-principle calculations, on the photogeneration of HCs[45-48] and their photocatalytic role[49-51] in the steady state. In parallel, the femtosecond dynamics of HCs can be readily examined, typically via optical means, by employing ultrashort optical pulses to photoexcite the metallic NP[52, 53]. However, reports on the electron-adsorbate energy transfer and catalytic activities are mostly limited to flat surfaces[37, 54-56], representing a completely different landscape than nanostructures. Towards this direction, ref.[57] successfully combined a description of the HC dynamics in plasmonic nanostructures with a quantum formalism to describe the ultrafast transfer of energy to the adsorbate. Yet, the model did not include the impact of the latter on the former, i.e., neglected effects of transient spectral distortion of the carrier energy distribution and altered HC dynamics due to the energy exchange with the adjacent adsorbate. Moreover, the model proposed did not incorporate a spatial dependence of the HC population, which is a fair assumption in the case of small NPs, but poses some limitations when considering larger NPs or more complex geometries as, e.g., NPs with hot spots[58-60] or antenna-reactors[61, 62], which are known to outperform the conventional systems.
A modeling approach for ultrafast photothermal catalysis has also been proposed in ref.[40], which explored the light-induced thermal effects in the pulsed illumination regime. A time-resolved description of the optical heating in plasmonic arrays was successfully coupled with chemical microkinetic modeling to show the advantages of ultrafast thermal modulation of the NP active sites. While the results clearly indicate that the pulsed illumination can outperform the steady state, the model focussed on photothermal effects, disregarding any electronic contribution.
As such, despite the promising advances, a comprehensive description of the ultrafast dynamics of HCs and ensuing thermal effects across extended plasmonic nanostructures in the presence of adsorbed molecules resonantly accepting energy from the photoexcited electrons is still elusive.

Here, to integrate the distinct effects involved in plasmonic catalysis in a selfconsistent manner, we propose an original approach based on a rate-equation model of the ultrafast relaxation of nonequilibrium carriers, where the transfer of electrons to the molecule acts as an extra decay channel. Our method combines the well-established quantum formalism of inelastic electron scattering with 'hot' adsorbates (generating transient negative ions)[63, 64] with a semi-classical description of plasmonic HCs dynamics, resulting in a compact model able to track over energy, time, and space the evolution of the electronic energies and the photoinduced thermal gradients following femtosecond-pulse illumination. Moreover, the contributions to the reactivity arising from charge transfer and thermal effects can be disentangled and assessed upon changes in input variables such as pulse fluence and duration, photon energy, nanostructure dimension, and shape.
By applying our model to a few relevant reactions[57, 65, 66] we validate our results while elucidating and providing deeper insight into some mechanisms observed for the analyzed reactions based on their energy landscape. Specifically, we predict wavelength-dependent reaction rates due to the hot carriers with the highest energies, as well as rates varying non-trivially with the pulse duration due to the spatio-temporal dynamics and inherent nonlinearities of both carriers close to the Fermi level and the NP lattice temperature. As a whole, the presented model provides a comprehensive, selfconsistent picture of the main processes of energy exchange between photoexcited plasmonic nanostructures and molecular adsorbates and offers a powerful tool to study light-driven chemical events in the temporal regime down to the ultrafast timescales.

Results and Discussion

Figure 1 provides a schematic overview of the typical system under investigation with its nonequilibrium photophysics, and illustrates our modeling approach for the description of the main mechanisms at play. In

particular, Fig. 1a depicts a metallic nanoparticle interacting with a molecular species (e.g., in its gas phase, as it happens in heterogeneous catalysis) upon illumination by an ultrafast optical pulse. Photoexciting the plasmonic NP generates[33, 45, 67]: (i) high-energy hot carriers, resulting from plasmon dephasing and producing nonequilibrium, short-lived (hundreds of fs to a few ps) electronic distribution $f(E)$; and (ii) an elevated temperature of the metal lattice within the NP (Θ_L), resulting from electron-phonon scattering events (occurring from a few to tens of ps) and subsequently heating the surrounding local environment. Both these processes can contribute to altering chemical reactions on the NP surface[30]. We refer to 'hot carriers' (HCs) to describe the nonequilibrium, higher-energy states of electrons and holes, including 'nonthermal' HCs (i.e., those with an energy spectrum differing from a Fermi-Dirac distribution) and 'thermalized' HCs (i.e., described by an effective elevated electronic temperature $\Theta_E > \Theta_0$, which fully determines their energy-dependent occupation via an out-of-equilibrium Fermi-Dirac distribution). Following pulsed photoexcitation, if electrons have transiently acquired sufficiently high energy to match an available state of the chemical species adsorbed onto the NP surface, a resonant transfer of energy can take place (inset in Fig. 1a). The process occurs on ultrafast timescales, and in the most general case, competes with electron relaxation. It can be interpreted as an inelastic scattering event between photoexcited HCs in the metal NP and the molecular system, leading, for example, to the desorption of the adsorbates,[64, 68] as sketched in Fig. 1b. More precisely, the process is triggered by a nonequilibrium mechanism where the HC from the metal NP (e.g., a hot electron as in Fig. 1b) transfers into the adsorbate, thus creating a transient negative ion (TNI)[28, 63, 69]. The TNI potential energy surface (PES, red curve in Fig. 1b) typically has a different minimum than the ground state PES (black curve in Fig. 1b) along a specific reaction coordinate (for desorption, this is the distance from the surface). This causes the TNI state to follow new reaction trajectories on the excited PES, determined by the TNI PES slope over a characteristic time τ_{TNI}. The adsorbate then returns to the ground PES in a vibrationally excited state, and the HC is scattered back to the NP with decreased energy. If the HC energy transfer into the adsorbate surpasses the activation energy (E_A), it can trigger a chemical reaction. More generally, the TNI mechanism could apply to reactions besides desorption, including diffusion[37, 66] and dissociation[70-72], which our model also could describe. The electronic process contributes to the chemical activity synergistically with photothermal effects, in which the light-induced lattice temperature increase brings the adsorbate to a vibrationally excited state within the ground PES, possibly overcoming the activation barrier E_A.

To describe the rich landscape of intertwined ultrafast mechanisms plasmonic HCs undergo, we propose a modeling approach starting from a rate-equation, thermodynamical description of the ultrafast energy exchange in photoexcited plasmonic nanostructures known as the Extended Two-Temperature Model (E2TM). The E2TM, initially proposed in ref.[73] and subsequently shown to accurately reproduce experimental investigations of femtosecond dynamics in various metallic systems[74, 75], considers the out-of-equilibrium metal as an ensemble of three coupled energy reservoirs: (i) the thermal electrons, energetically described by a temperature Θ_E and corresponding Fermi-Dirac distribution, (ii) the phonons of the metal lattice, at temperature Θ_L, and (iii) a fraction of non-thermalized electrons described in terms of a suitable occupation probability variation with respect to the equilibrium one, Δf_{NT}. More details are provided in the Methods section, as well as in refs.[73, 76, 77] and references therein. In the model we present here, we expand the E2TM, and hence referred to as the Generalized E2TM (GE2TM), by introducing additional electronic relaxation channels to account for the interaction with hybridized TNI states in the adsorbate. To better visualize the rationale of our model, Fig. 1c presents a Sankey diagram showing an overview of how energy flows through the different channels in the GE2TM, specifically delineating the various electron de-excitation channels integral to our proposed approach. This figure serves as a comprehensive guide to illustrate the interrelated processes involved in our modeling framework.

The proposed GE2TM solves for the three coupled equations describing the nonthermal HCs, thermal HCs, and lattice temperature of the plasmonic NP, respectively, represented by Δf_{NT}, Θ_{E}, and Θ_{L}, which reads as follows:

$$\frac{\partial \Delta f_{\mathrm{NT}}(\mathbf{r},t,E)}{\partial t} = -\frac{\Delta f_{\mathrm{NT}}}{\tau_{ee}} - \frac{\Delta f_{\mathrm{NT}}}{\tau_{ep}} + R_{\mathrm{abs}}(\mathbf{r},t,E) - R_{\mathrm{int}}(\mathbf{r},t,E), \tag{1a}$$

$$C_{\mathrm{E}}\frac{\partial \Theta_{\mathrm{E}}(\mathbf{r},t)}{\partial t} = -\nabla\cdot(-\kappa_{\mathrm{E}}\nabla\Theta_{\mathrm{E}}) - G(\Theta_{\mathrm{E}}-\Theta_{\mathrm{L}}) + \frac{\partial U_{ee}^{\mathrm{NT}}(\mathbf{r},t)}{\partial t} - Q_{\mathrm{int}}(\mathbf{r},t), \tag{1b}$$

$$C_{\mathrm{L}}\frac{\partial \Theta_{\mathrm{L}}(\mathbf{r},t)}{\partial t} = \kappa_{\mathrm{L}}\nabla^2\Theta_{\mathrm{L}} + G(\Theta_{\mathrm{E}}-\Theta_{\mathrm{L}}) + \frac{\partial U_{ep}^{\mathrm{NT}}(\mathbf{r},t)}{\partial t} \tag{1c}$$

As indicated by the labels in Fig. 1c, Eq. 1a governs the spatial and energy-dependent dynamics of the nonthermal HC distribution, with the terms on the right-hand side describing, respectively, the change in electronic population due to electron-electron (*ee*) scattering (with a rate $1/\tau_{ee}$), electron-phonon (*ep*) scattering (with a rate $1/\tau_{ep}$), absorption, and the interaction with the chemical species. The other two equations describe the spatial dependent dynamics of the electronic and lattice temperatures, respectively, accounting for spatial diffusion (via a Fourier-like term), the coupling between thermalized electrons and the lattice (via the coefficient G), and the source of energy from the relaxation of nonthermal HCs, coupled both to thermalized electrons (phonons) through *ee* (*ep*) scattering events. Similarly to the nonthermal case, the thermalized electrons are also able to inject energy into the adsorbates through a term $Q_{\mathrm{int}}(\mathbf{r},t)$. While we consider the occurrence of chemical reactions due to the lattice temperature increase at the nanoparticle surface (through an Arrhenius term), we ignore the negligible cooling of the surface from this energy transfer (depicted in Figure 1c by the monodirectional arrow from the lattice to the injection for catalysis).

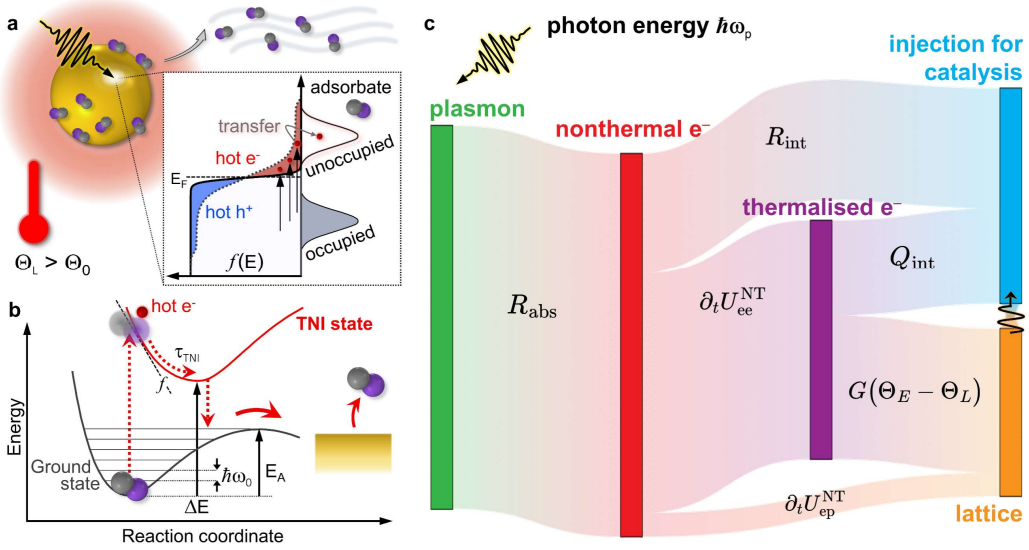

Fig. 1: Schematics of the modeling approach. **a)** Sketch of the system under study. An ultrafast light pulse photoexcites a metallic nanostructure, resulting in a nonequilibrium electronic population $f(E)$ and a NP lattice temperature (Θ_{L}) increase. From their photoexcited states, hot electrons and holes can transfer energy to the unoccupied states of chemical species adsorbed onto the NP surface, thus promoting chemical transformations (e.g., bond breaking). According to the Arrhenius equation, the NP lattice temperature also promotes chemical reactions. **b)** Schematic of the mechanism for electron energy deposition into an adsorbate. The inelastic scattering between photoexcited electrons and molecular states produces an electronic excitation of the adsorbate, which evolves along an excited TNI PES to return to the ground state PES in a vibrationally excited state. With sufficient excess energy to

overcome the activation energy E_A, the reaction (here, desorption as an example) occurs. **c)** Sankey diagram of the proposed modeling approach, visually depicting the flows of energy through the electron de-excitation channels involved in the GE2TM.

Complete details of the terms appearing in the GE2TM, inherited by the E2TM, are provided in the Methods section and previous reports[73, 74, 77]. The adsorbate interaction term for nonthermal HCs, R_{int}, is derived from the quantum formalism of TNI states through the following expression:

$$R_{\mathrm{int}}(\mathbf{r},t,E) = \frac{-1}{\tau_{\mathrm{surf}}}\sum_n [\Delta f_{\mathrm{NT}}(\mathbf{r},t,E+n\hbar\omega_0)P_n(E+n\hbar\omega_0) - \Delta f_{\mathrm{NT}}(\mathbf{r},t,E)P_n(E)]. \quad (2)$$

In essence, the quantum calculations we implemented following previous reports[57, 65, 66] require, as input, the following quantities: the TNI PES slope f, the ground state vibrational spacing $\hbar\omega_0$, the energy separation between the ground and TNI states ΔE the average lifetime of the TNI state τ_{TNI}, and the activation energy E_A, all illustrated in Fig. 1b. The calculation yields the probability, $P_n(E)$, that an electron with energy E that scatters off the adsorbate will lose n vibrational quanta of energy upon interacting with it. Additionally, the interaction rate should also depend on the probability that an electron reaches the metal surface, i.e., where the energy transfer to the adsorbed chemical species may occur. We estimated this quantity by assuming, following ref.[78], that all the electrons, on average (i.e., regardless of their spatial position within the NP), reach the NP surface and scatter off the adsorbate on a nanostructure geometry-dependent timescale τ_{surf}. In particular, this quantity is expressed as the ratio between an effective length (accounting for the geometry of the nanoparticle) and the material-specific Fermi velocity. For the scope of the present work, we will use τ_{surf} as a leading-order estimate of the surface scattering rate, and more sophisticated expressions (e.g., including space and energy dependence) will be investigated in the future. An expression equivalent to Eq. 2 holds for thermalized HCs and the corresponding term for injection Q_{int}, where the variation in the electronic population is due to a perturbed Fermi-Dirac distribution, i.e., $\Delta f_T = f_{FD}(E, \Theta_E) - f_{FD}(E, \Theta_0)$. Note that the quantum formalism implemented, which follows the Menzel-Gomer-Redhead desorption model[79, 80], is not the only option to describe the electronic energy transfer. In principle, different approaches could be used to express the terms R_{int} and Q_{int} of the GE2TM, as long as they provide an estimate of the probability for an electron to interact with the adsorbate.

With this set of definitions and expressions at hand, we implemented our GE2TM in a Finite Element Method (FEM)-based simulation environment, which creates a powerful numerical platform suited to describe with space, time, and energy resolution the ultrafast dynamics and energy injection of plasmonic hot carriers in nanostructures of arbitrary complexity. As relevant reactions, we examine the molecular processes of desorption of NO and the diffusion of O on a platinum nanoparticle (Pt(111) surfaces, assuming a 1/4 monolayer of the adsorbed species) using the TNI parameters reported in ref.[57], noting that our approach could be applied to virtually any system.

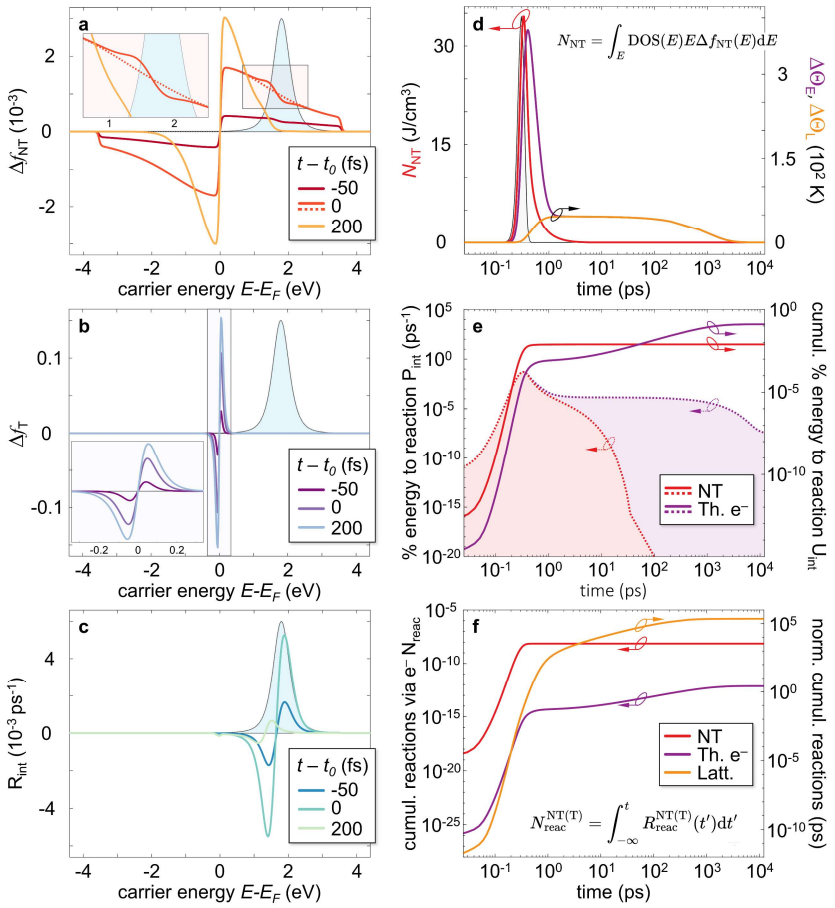

Fig. 2: Simulating the ultrafast dynamics of plasmonic hot carriers in the presence of an adsorbate. Results of the GE2TM for the case of a single Pt nanosphere (radius 5 nm) promoting NO desorption. A pulse with duration (full width at half maximum in intensity) Δt = 100 fs centered at t_0 = 300 fs, fluence F_p = 1 mJ/cm^2, at a wavelength of λ_p = 350 nm (photon energy $\hbar\omega_p \approx 3.54$ eV) is incident. **a)** Energy distribution of the nonthermal portion of the hot carrier population Δf_{NT} at a delay of –50 fs, 0 fs, and 200 fs (from darker to lighter red shades) from the exciting pulse peak t_0. The (normalized) probability $P_1(E)$ of energy transfer to NO via electron inelastic scattering is shown (light blue shaded area). The solution of the GE2TM without interaction term (i.e., in the absence of a de-excitation channel for electrons towards an adsorbate) is also depicted for the 0-fs delay (dotted line) The panel inset shows a zoomed-in of the spectral distortion of Δf_{NT} introduced by the interaction. **b)** Energy distribution of the thermalized hot carrier population Δf_T at a delay of –50 fs, 0 fs, and 200 fs (from darker to lighter purple shades) from the exciting pulse peak t_0. The panel inset shows a zoomed-in view around the Fermi level E_F. **c)** Energy distribution of the interaction term $R_{int}(t,E)$ modeling the inelastic scattering mechanism that regulates the energy transfer from the nonequilibrium carrier population to the adsorbate. **d)** Temporal dynamics of the internal energetic degrees of freedom for the photoexcited plasmonic NP: $N_{NT}(t)$, the total energy stored in the nonthermal fraction of the HC population (red, left axis); $\Delta\Theta_E(t)$, the electronic temperature increase (purple, right axis); $\Delta\Theta_L(t)$, the lattice temperature increase (orange, right axis). The (normalized) temporal profile of the exciting pulse is also shown (shaded grey area). **e)** Temporal dynamics of the instantaneous (dotted lines and shaded areas, left axis) and cumulative (solid lines, right axis) percentage of energy (normalized to the absorbed energy) of nonthermal (red) and thermalized (purple) electrons transferred into the adsorbate. **f)** Temporal dynamics of the cumulative number of reactions induced by nonthermal (red, left axis) and thermalized (purple, left axis) electrons, assuming an energy threshold for NO desorption expressed as $n_{reac}\hbar\omega_0 > E_A = 1.29\,eV$, which occurs for $n_{reac} = 7$, following ref.[57]. The dynamics of the cumulative contribution due to the lattice temperature increase according to the Arrhenius law (normalized to the rate at room temperature) is also shown (orange, right axis).

We now present a relevant example to highlight the predictive capabilities of the model and showcase the typical outcomes and available quantities computed. Figure 2 shows the results obtained for a single Pt nanosphere with a radius of 5 nm, acting as a catalyst in promoting NO desorption, similar to the case-study system examined in previous reports[57]. Exploiting axial symmetry, simulations were conducted in 2D, employing a semicircle to mimic the response of the nanosphere and assuming a spatially homogeneous absorption within the NP, given its small size. We consider an ultrafast optical pulse with a duration (full width at half maximum in intensity) of Δt = 100 fs, centered at t_0 = 300 fs, and fluence (F_p) of 1 mJ/cm² at a wavelength (λ_p) of 350 nm (photon energy $\hbar\omega_p \approx 3.54$ eV). In Fig. 2a, the ultrafast evolution of the nonthermal portion of the HC population (Δf_{NT}) is shown. Their energy distributions are depicted at different time delays from the peak of the exciting pulse, as indicated in the legend. For reference, the normalized probability, $P_1(E)$, of energy transfer into NO via electron inelastic scattering is shown (shaded area), highlighting the strongly energy-dependent impact of the de-excitation channel for electrons towards the adsorbate. Clearly, near the peak of this probability (at ~1.8 eV for NO), the nonthermal electron population develops a dip as energy is transferred into the chemical species, while an excess population develops at approximately $\hbar\omega_0$ lower in energy. This is the fingerprint of vibrational energy transfer from nonequilibrium HCs to the chemical species. The effect is more apparent when the estimated Δf_{NT} is compared to its counterpart computed in the absence of the adsorbate interaction term. Specifically, the dotted curve shows the solution obtained in the absence of the chemical species, which does not exhibit any spectral distortion close to the peak of $P_1(E)$. As expected, the electron transfer into the adsorbate competes with electronic relaxation, as shown by comparing the spectra of Δf_{NT} at the pulse peak (orange shade) and at longer delays (200 fs, darker red shade), i.e., when, following *ee* scattering, the higher-energy electrons are brought back closer to the Fermi level on ultrafast timescales. In principle, the same energy transfer mechanism also occurs for thermal HCs. Figure 2b shows the ultrafast evolution of the thermalized electron population (Δf_T). The inset shows a zoom-in around the Fermi level (E_F) for increased visibility. In this case, no impact of the adsorbate de-excitation channel on the evolution of Δf_T is observed. This is due to the energy difference between the hot electrons and the adsorbate resonance. Our calculations provide direct insight into the evolution of the interaction terms, evolving in time and electronic energy based on the nonequilibrium states involved in the adsorbate excitation. In particular, Fig. 2c analyzes the interaction term that models the inelastic scattering for nonthermal HCs, $R_{int}(t, E)$. The observed peculiar energy spectrum, consisting of a dip (peak) at lower (higher) energies, stems directly from the character of the injection mechanism, where electrons scatter off the adsorbate, lose a fraction of their initial energy $\hbar\omega_0$, and then return to the metal. By inspecting the energy distribution of this term at the same time delays as in the previous panels, the simulations show that in agreement with what was predicted for electrons, $R_{int}(t, E)$ changes in amplitude throughout the photoexcitation and tends to shift towards the Fermi level while electrons progressively decrease their high-energy content via *ee* relaxation.

To track more closely the ultrafast dynamics of the nonequilibrium state of the plasmonic NP, in Fig. 2d, we show the temporal evolution over a long time interval of the total energy density stored in the nonthermal HCs (red curve, left axis) along with the temperature increase of the thermalized HCs (purple curve, right axis) and the lattice temperature increment (orange curve, right axis). The exciting pulse profile is also overlaid for reference (black curve). We observe that nearly all the nonthermal HCs have relaxed back to equilibrium within ~1 ps of delay from the pulse peak, while the thermalized HCs and the lattice take ~3 ps to thermalize with each other. These dynamics are mostly consistent with the ones typically observed in plasmonic systems[52]. Eventually after a few nanoseconds, the distributions thermalize with the environment. Similarly, from the standpoint of the ultrafast energy transfer, Fig. 2e reports the temporal dynamics of the instantaneous (dotted curves) and cumulative percentages (solid curves) of the energy transferred into the adsorbate by nonthermal (red curves) and thermalized electrons (purple curves).

Interestingly, these quantities effectively highlight, even for the simple case here examined, how the two different kinds of carriers contribute differently to the reaction, with thermal HCs overtaking the nonthermal ones when, after a few hundred fs, *ee* scattering has made the latter vanish.
Besides information on the electronic populations and the ultrafast dynamics of internal energetic degrees of freedom, our model allows for estimating experimentally accessible quantities directly related to the chemical transformation induced at the metal NP surface. In Fig. 2f, we show the cumulative number of reactions induced by nonthermal (red curve, left axis) and thermalized electrons (purple curve, left axis), considering the activation energy for NO desorption. Furthermore, the differential contribution (i.e., with respect to room temperature) due to the lattice temperature increase, following the Arrhenius law, is presented (orange curve, right axis, normalized to the reactivity at room temperature).
Note that our model considers reactions to be instantaneous after the adsorbate energy exceeds the activation barrier and does not track the dynamics of the vibrationally excited state of the adsorbate. While this is a fair assumption for NO desorption[57, 81], including a more detailed description of the molecule dynamics may be of great relevance, especially when the considered reactions require nano- to microseconds to occur[82].
By resolving the cumulative number of reactions over time into electronic and phononic contributions, it can be noted that the contributions substantially follow the dynamics of the corresponding energetic degree of freedom (Fig. 2d, same color coding). First, following impulsive ultrafast illumination, nonthermal electrons contribute to depositing energy into the adsorbate and quickly reaching a plateau in reaction number. Thermal electrons are then excited within the first ps, and the number of reactions activated by the increased electronic temperature rises until complete relaxation. A similar behavior is predicted for the lattice temperature contribution, yet with slower dynamics, mainly boosted when *ep* scattering becomes more effective.
This comprehensive analysis of the results obtained by solving the GE2TM offers valuable insights into the intricate interplay between hot carrier dynamics and catalytic processes, setting the stage for a deeper understanding of light-driven chemical transformations. Besides, the numerical platform implemented here allows for examining any interaction conditions by adjusting the geometry and active material of the nanostructure, the optical pulse parameters, and the monitored reaction. The impact of such parameters on the chemical reactivity can be assessed quantitatively and rationalized in terms of distinct contributions arising from the main energetic degrees of freedom (nonthermal HCs, thermalized HC, and the lattice) of the plasmonic NP.

To further illustrate the chemistry that can occur, we analyzed the effects of (i) changing adsorbate energetics by driving different chemical reactions on the photoexcited NP surface and (ii) varying the exciting pulse wavelength λ_p. In particular, Figure 3 provides a detailed exploration of the outcomes generated by the GE2TM for an individual Pt nanosphere (radius 5 nm), focusing on its catalytic role in either NO desorption (left panels, same reaction as Fig. 2) or O diffusion (right panels) with respect to a varying pulse photon energy. In Fig. 3a, the spectral distributions of the nonthermal portion of the HC population (Δf_{NT}, red shades, left axis) and thermal HCs (Δf_T, purple shades, right axis) are depicted at the peak of the exciting pulse (0 fs delay) for three distinct pulse wavelengths λ_p of 400 nm (solid), 600 nm (dotted), and 800 nm (dash-dotted). Note that we normalize these quantities to the NP absorption efficiency (Q_{abs}) at the corresponding pulse wavelength to make them more comparable.

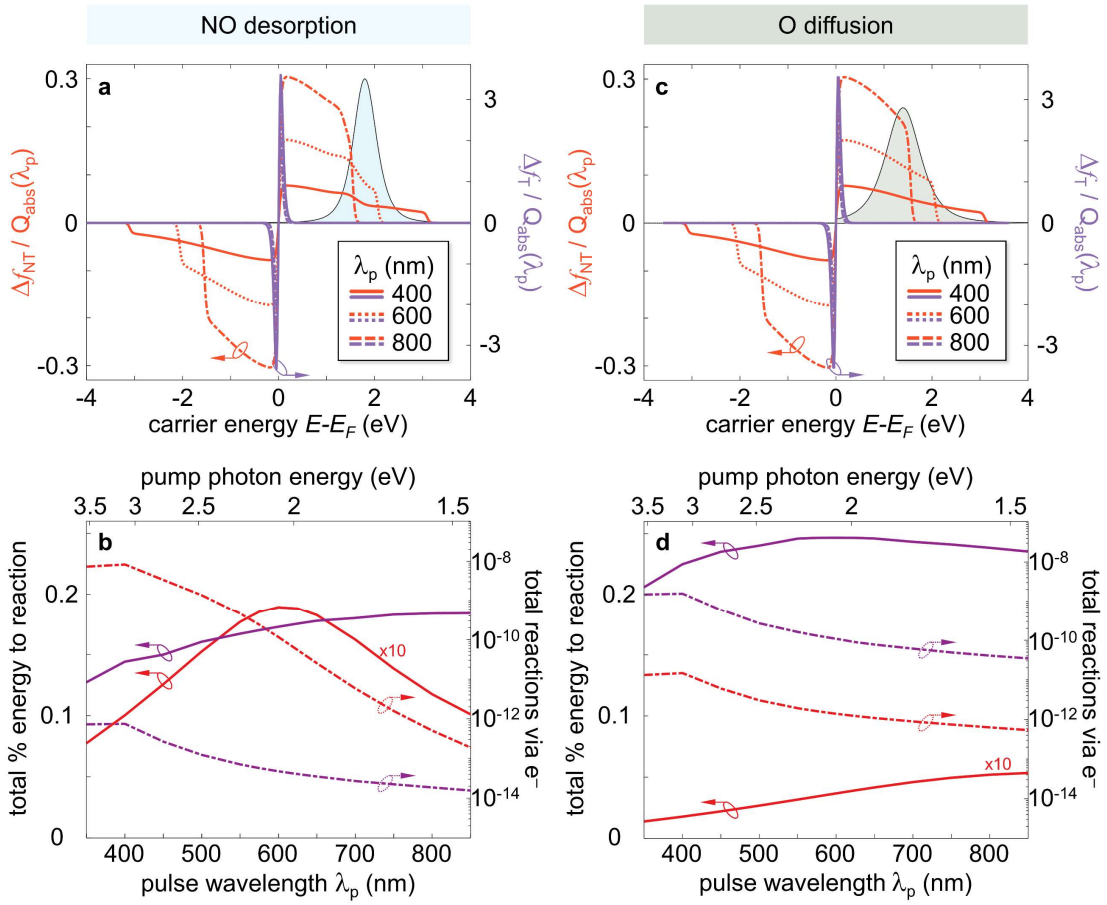

Fig. 3: Ultrafast hot carriers in Pt nanosphere for different photon energies. Results of the GE2TM for the case of a single Pt nanosphere (radius 5 nm) promoting either NO dissociation (left panels) or O diffusion (right panels) as a function of the exciting pulse photon energy. **a)** Energy distribution of the nonthermal portion of the hot carrier population Δf_{NT} (red shades, left axis) and of the thermal hot electrons Δf_{T} (purple shades, right axis) at a delay of 0 fs from the exciting pulse peak t_0, for pulse wavelengths λ_p of 400 nm (solid), 600 nm (dotted) and 800 nm (dash-dotted). The changes in electron distributions are normalized to the NP absorption efficiency Q_{abs} at the corresponding pulse wavelength. The (normalized) probability $P_1(E)$ of energy transfer to NO via electron inelastic scattering is shown (light blue shaded area). **b)** Left axis: total percentage of energy (normalized to the absorbed energy) of nonthermal (red solid, magnified by a factor of 10 for better reading) and thermalized (purple solid) electrons transferred into the adsorbate as a function of the pulse wavelength. Right axis: total number of reactions induced by nonthermal (red dash-dotted) and thermalized (purple dash-dotted) electrons as a function of the pulse wavelength. **c-d)** Same as (a)-(b) respectively, for O diffusion.

Additionally, the light blue shaded area represents the normalized probability $P_1(E)$ of energy transfer to NO via electron inelastic scattering. Consistent with our description of HC photogeneration[73, 74] (see also the Methods section), excited electrons reach states with energies as high as $E_F + \hbar\omega_p$. As such, longer pulse wavelengths lead to less broad energy distribution of HCs (compare red solid and dash-dotted lines in Fig. 3a). In the framework of promoting catalysis, this relation is an extra knob for tailoring the energy overlap between HCs and adsorbate states, hence promoting or hindering the transfer. The optimal flow of energy to the molecular system is expected for a maximized overlap.

In this regard, in Fig. 3b, the left axis illustrates the total percentage of energy (normalized to the energy absorbed by the NP) of nonthermal (red solid, magnified by a factor of 10 for clarity) and thermalized (purple solid) electrons transferred into the adsorbate (a NO molecule) as a function of pulse wavelength, while the right axis portrays the total number of reactions induced by nonthermal (red dash-dotted) and thermalized (purple dash-dotted) electrons over the pulse wavelength range. By inspecting the wavelength-dependence of these quantities, the energy transfer from nonthermal HCs (solid red) exhibits a resonant trend with a maximum peaking at ~600 nm (~2 eV) as a result of the mechanism outlined above regarding the overlap between Δf_{NT}, and $P_1(E)$. The same does not hold for thermal electrons, whose distribution Δf_T remains mostly localized around E_F regardless of the pulse photon wavelength. The energy transferred into the adsorbate increases with increasing λ_p, but with a non-resonant profile. Despite these differences between nonthermal and thermal HCs in the energy transfer (Fig. 3b left axis), the cumulative number of reactions induced (Fig. 3b right axis) exhibits a similar trend with pulse wavelength. These quantities (dash-dotted lines) mostly follow the spectral shape of the NP absorption efficiency (shown in Fig. S1), which ultimately dictates the amount of energy entering the system. While this effect dominates the observed spectra of the reactions induced by electronic energy, the (albeit minor) distortion of the curve referring to nonthermal HCs (red dash-dotted) compared to the thermal electron one (purple dash-dotted) is indeed understood as resulting from the optimal energy transfer for a 600 nm pulse. Figure 3c and 3d mirror the format of Figs. 3a and 3b, respectively, but focus on O desorption. Notably, the non-resonant spectrum of the percentage of energy from nonthermal electrons to the adsorbate (red solid curve) in Fig. 3c stands in stark contrast to the corresponding result for NO desorption, Fig. 3b, underscoring the diverse catalytic behaviors resulting from different photon energies. Given the energetics of O diffusion, whose $P_1(E)$ has a peak at approximately 1.4 eV, i.e., closer to E_F, any pulse photon energy in the visible range provides a comparable overlap with Δf_{NT}, resulting in a non-resonant profile of the energy transferred from nonthermal electrons. As for NO, the thermal electron contribution (solid purple) shows a trivial dependence on the pulse photon energy. This, in turn, causes the two curves for the cumulative number of reactions (dash-dotted, right axis) to exhibit the same dependence on λ_p, precisely reproducing that of the plasmonic nanosphere absorption cross-section. Overall, our model provides predictions that are consistent with the results obtained with similar numerical techniques[57], while expanding the capabilities of previous approaches thanks to the fully selfconsistent coupling between the electron spatio-temporal dynamics, the resonant interaction with the adsorbate, which distorts the electronic distribution, as well as including the lattice heating.

The small spherical Pt nanoparticle represents a system that could be described as a 2D problem. We now move to a more complicated geometry, a 3D bowtie nanoantenna. This geometry is selected because it can produce a highly localized absorption spatial pattern with resonant hot spots[83, 84]. The study of this system will highlight the impact of electronic spatial inhomogeneities and intra-particle (electronic and phononic) diffusion in the model[85-87]. Figure 4 summarizes the results from the GE2TM applied to a Pt bowtie, with a length (L_x) of 45 nm, height (H_z) of 5 nm, width (W_y) of 20 nm, and a 5 nm gap. Focusing on the light-driven promotion of NO desorption, simulations are conducted in 3D, for a pulse with duration of Δt = 100 fs centered at t_0 = 300 fs. The pulse has a fluence (F_p) of 75 μJ/cm², a wavelength λ_p of 600 nm ($\hbar\omega_p \approx 2.06$ eV), and is linearly polarized along the bowtie (x-) axis, impinging at normal incidence (i.e., along the z-axis). The NP geometrical parameters were adjusted to tune the plasmonic bowtie resonance to the pulse wavelength, at which the light absorption pattern exhibits a strongly inhomogeneous spatial pattern with enhanced near fields localized at the tips (see Fig. S2). Throughout the ultrafast optical illumination, the same pattern (encoded in the term R_{abs} in our model) is inherited by nonthermalized HCs first (their diffusion is neglected in the GE2TM, as it would be expected to occur on timescales comparable with their ultrafast relaxation), then by thermal HCs, which diffuse across the NP[85]. Figure 4a illustrates the

space-dependent effects of the photoexcitation by displaying the spatial distribution across the plasmonic bowtie of the total energy density stored in nonthermal electrons (N_{NT}) on the left and the electronic temperature increase ($\Delta\Theta_E$) on the right, both evaluated at the exciting pulse peak t_0. Besides their spatial dependence, these quantities also evolve in time over ultrafast timescales, as illustrated in Fig. 4b, where we show the temporal dynamics of internal energetic degrees averaged over the bowtie volume, including N_{NT} (red, left axis), $\Delta\Theta_E$ (purple, right axis), as well as $\Delta\Theta_L$ (orange, right axis). The normalized temporal profile of the exciting pulse is overlaid with a grey curve. Note that, compared to what was observed in the previous case of a small nanosphere (Fig. 2), the system reaches much higher nonequilibrium states, with the nonthermal electron energy ~2 orders of magnitude larger than for the sphere (compare with Fig. 2d), the electronic temperature as high as ~1800 K, and the lattice temperature reaching up to ~500 K. Such high transient levels of excitation and temperatures (of both electrons and phonons) reached on ultrafast timescales enables several nonequilibrium mechanisms otherwise unattainable. For instance, considering a continuous-wave illumination with the same average power as the pulse, much lower temperature increases of only ~3 K are obtained. This result clearly shows the potential for ultrafast pulsed catalysis. The electron-phonon equilibration is achieved within a few ps, in agreement with previous reports[52], while the total relaxation (equilibration with the surrounding environment) requires a few ns.

Additionally, the model allows for accessing each quantity of interest locally, i.e., at arbitrary positions around the nanoparticle. The energy content of nonequilibrium electrons, the occupancy distribution variations of the nonthermal portion of the hot carrier population (Δf_{NT}) and thermalized hot electrons (Δf_T) are shown in Fig. 4c close to the bowtie tip, with the (normalized) probability of energy transfer to NO via electron inelastic scattering also presented as a light blue shaded area. As for the nanosphere (Fig. 2), Δf_{NT} is distorted due to the inelastic scattering with the adsorbate (see orange curve), a mechanism competing with relaxation, which tends to bring electrons closer to the Fermi level. Moreover, for the bowtie and the present interaction conditions considered, and especially given the high electronic temperature, Δf_T is more spread out in carrier energy than in the sphere case. This increases the energy overlap with $P_1(E)$ and is expected to enhance the contribution to the reaction due to thermalized HCs.

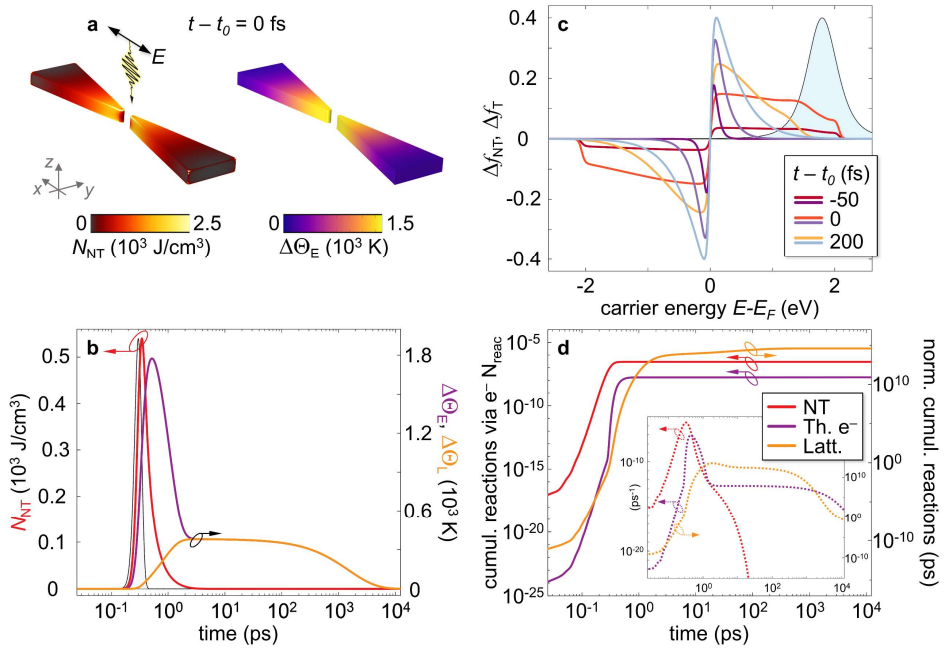

Fig. 4: Simulating the ultrafast dynamics of plasmonic hot carriers in the presence of an adsorbate across designer nanostructures. Results of the GE2TM for the case of a single Pt bowtie (length L_x = 45 nm, height H_z = 5 nm, width W_y = 20 nm, and a 5 nm gap between them) promoting NO desorption. A pulse with a duration (full width at half maximum in intensity) Δt = 100 fs centered at t_0 = 300 fs, fluence F_p = 75 μJ/cm^2, at a wavelength of λ_p= 600 nm (photon energy $\hbar\omega_p \approx$ 2.06 eV), linearly polarised along the bowtie (*x*-) axis and impinging at normal incidence (*z*-axis) is considered. **a)** Spatial distribution of the total energy density stored in the nonthermal electrons N_{NT} (left) and of the electronic temperature increase $\Delta\Theta_E$ (right) at the exciting pulse peak t_0. **b)** Temporal dynamics of the internal energetic variables of the photoexcited plasmonic NP, averaged over its volume: N_{NT} (red, left axis), $\Delta\Theta_E$ (purple, right axis), $\Delta\Theta_L$ (orange, right axis). The (normalized) temporal profile of the exciting pulse is also shown (grey shaded area). **c)** Energy distribution variations of the nonthermal portion of the hot carrier population Δf_{NT} (red shades) and of the thermalized hot electrons Δf_T (purple shades) evaluated at a position close to the bowtie tip at time delays of –50 fs, 0 fs, and 200 fs (from darker to lighter shades) from the exciting pulse peak t_0. The (normalized) probability $P_1(E)$ of energy transfer into NO via electron inelastic scattering is shown (light blue shaded area). **d)** Temporal dynamics of the cumulative number of reactions induced by nonthermal (red, left axis) and thermalized (purple, left axis) electrons, averaged over the NP volume. The dynamics of the cumulative contribution due to the lattice temperature increase according to the Arrhenius law (normalized to the rate at room temperature) is also shown (orange, right axis). The panel inset shows the temporal dynamics of the corresponding instantaneous reactions rates (averaged over the NP volume) for the electrons (nonthermal and thermal, left axis, in ps^{-1}) and the lattice (normalized to the Arrhenius-like rate at room temperature).

Lastly, Fig. 4d displays the time evolution of the cumulative number of reactions induced by nonthermal and thermalized electrons, averaged over the NP volume. Additionally, the cumulative contribution due to the lattice temperature increase according to the Arrhenius law (normalized to the rate at room temperature) is presented on the right axis. Our calculations predict that the electronic terms (red, purple) reach a plateau relatively quickly and then relax back to equilibrium with energy flows to the lattice. As a result, the phonon contribution (relative to the room temperature reactivity) is delayed by a few ps. However, it then keeps increasing along the entire time interval considered (up to ns), with minor changes in lattice temperature affecting the reaction exponentially. Moreover, the inset in Fig. 4d details the instantaneous reaction rates (averaged over the NP volume) for both electrons (nonthermal and thermal, left axis, in ps^{-1}) and the lattice (normalized to the Arrhenius-like rate at room temperature, hence unitless). The results clearly suggest that each of these contributions dominates over distinct timescales, with purely electronic effects at the early stages following impulsive photoexcitation and the lattice temperature taking over at longer times. This feature, inherent to the pulsed illumination regime, could contribute to fundamental insights into the interplay of these effects.

To complete our investigation, we used our model to examine the effect of the exciting pulse temporal duration on the chemical reactivity for the two reactions considered (NO desorption and O diffusion on the Pt bowtie). In light of recent reports on the topic[38, 40], this analysis is of particular relevance, as it could shed light on the role of pulsed illumination and transient nonlinearities in light-driven chemistry beyond the stationary regime.
Figures 5a and Fig. 5b show, respectively, the total number of reactions of NO and O induced by the Pt bowtie (same geometrical parameters as before) under varying pulse durations, ranging from 100 fs to 1 ns. The other pulse parameters are the same as in Fig. 4, including the pump fluence, which implies that pulses with different durations feature the same total energy but are distributed differently in time.

We observe that, in both cases, the contributions from the nonthermal electrons (red curves) are constant with respect to the pulse duration. This is because (i) decreasing the pulse duration leads to higher peaks

over shorter durations (see Fig. S3) and (ii) multielectron processes are neglected, which is a reasonable assumption for the reactions considered here. By replacing our quantum formalism with other models, such as e.g., those considering the regime of desorption induced by multiple electronic transitions (DIMET)[88-90], our approach could be straightforwardly extended to more complex reactions. While a similar trend is obtained for the electronic temperature itself (featuring higher peaks over shorter durations; see Fig. S3 for further details), the nonlinear relation introduced by the Fermi-Dirac exponential connecting the electronic temperature and the carrier energy occupancy distribution allows, in principle, the thermal electronic contribution to vary with pulse duration. For the specific reactions considered here, this electronic nonlinearity is the main reason for the trend observed for NO desorption (Fig. 5a, purple line), where the number of reactions due to thermal hot carriers decreases with increasing pulse duration.

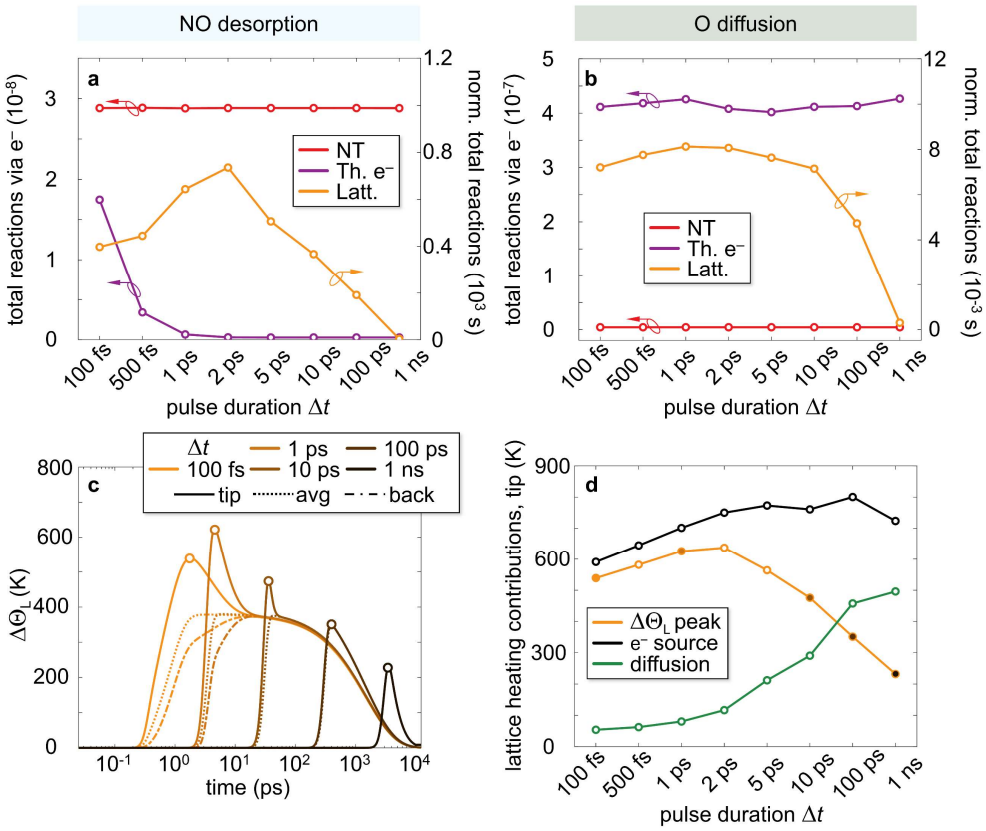

Fig. 5: Ultrafast hot carriers in Pt bowtie for varying pulse temporal duration. Results of the GE2TM for the case of a single Pt bowtie (same geometrical parameters and illumination conditions as in Fig. 4) as a function of the temporal duration Δt of the exciting pulse, varied while conserving the pulse fluence (F_p = 1 mJ/cm^2). **a)** Total number of NO desorption reactions induced by nonthermal (red, left axis) and thermalized (purple, left axis) electrons averaged over the NP volume for varying pulse durations. The total number of reactions due to the lattice temperature increase according to the Arrhenius law (normalized to the rate at room temperature, hence in units of *s*) averaged over the nanoparticle surface (orange, right axis). **b)** Same as (a) for O diffusion reactions. **c)** Temporal dynamics of the lattice temperature increase (NO desorption) evaluated at a position close to the bowtie tip (solid), far from the tip at the bowtie back (dash-dotted), and averaged over the NP volume (dotted) for varying pulse durations. **d)** Analysis of the terms involved in the dynamic lattice heating (see Eq. 1c), evaluated locally at a position close to the bowtie tip (NO desorption). The peak of the lattice temperature increase [marked by colored points in panel (c)] as a function of the pulse duration (yellow) is compared with the cumulative heating source up to the time of the corresponding temperature peak resulting from electron relaxation (black) and the dissipation term resulting from heat diffusion (green).

While this behavior is very prominent for NO desorption, it is almost absent when O diffusion is considered (Fig. 5b, purple line). This difference is due to the different dynamics (see Fig. S4) and energetics of the two reactions. For NO (with the peaks of $P_n(E)$ at higher energies[57]), the reactions occur only in the presence of a large Θ_E and the onset of the electronic nonlinearities is at ~500 K, as we show in Fig. S4. This implies that most of them happen in time near the peak of the electronic temperature, which, here, exceeds thousands of K (see Fig. S3), and are therefore strongly dependent on the peak value reached. Conversely, O diffusion (lower energy transfer probabilities) does not require particularly high electronic temperatures to occur, and the nonlinearity of the electronic temperature is displayed for Θ_E>~600 K. Therefore, most reactions happen on longer timescales when the electronic temperature increase is only ~400 K, which is in the linear regime, yet it remains at this value for a longer time. The further major difference in the electronic contributions between the two reactions is the relative weight of the term due to nonthermal carriers compared to that arising from thermalized electrons. For NO desorption (Fig. 5a), nonthermal carriers dominate, while they provide only a small contribution to O diffusion. Consistent with what is observed in Fig. 3, this effect can be rationalized by considering the distinct energetics of the adsorbates, which produce a different overlap in energy between the transfer probability and the nonequilibrium electron population. Interestingly, the contribution from the lattice (yellow curves) displays a peak around 1-2 ps pulse durations for NO desorption Δt Fig. 5a) and then decays for increasing Δt. For very long pulses ~1 ns, the peak lattice temperature decreases because, on those timescales, the particle loses heat to the environment. On the other hand, to explain the trend at shorter pulse durations, the intra-particle ultrafast heat diffusion across the bowtie needs to be considered. In particular, for NO desorption in Fig. 5c we show the local dynamics of the lattice temperature at two positions, near the tip of the bowtie (solid curves) and its back (dash-dotted curves), as well as the volume average over the entire particle (dotted curves) for various pulse durations (increasing from lighter to darker color shades). The lattice temperature increases up to a peak (more pronounced for shorter pulses) and then slowly decreases back to equilibrium on longer timescales. By varying the pulse duration, the peak temperature (marked by circles in Fig. 5c) is not monotonic and tends to increase up to the case with 1 ps pulse Δt, then decrease for longer pulses. The origin of this effect lies in the local interplay between the source for the temperature increase and its dissipation term, respectively, electron relaxation and heat diffusion (see Eq. 1c). More precisely, in Fig. 5d, we track the maximum lattice temperature increase at the tip for various pulse durations (yellow curve, made up by collecting the peaks of Fig. 5c, see white circles with same color coding). The black and green curves display, respectively, the amount of heat that has locally entered (black) and left (green) that position due to heating from electron-phonon exchange and cooling from diffusion. Although both quantities tend to increase with Δt, their difference, which ultimately determines the lattice temperature, displays a peak. This is because of the interplay between the timescales of heating, which is determined by the pulse duration, and cooling, influenced by the geometry and material properties. At the tip location, and for increasing pulse durations, lattice heat diffusion lags with respect to the *ep* scattering-driven heat input, yielding an optimum corresponding to a peak in the lattice temperature.

In addition, differently from the tip position, the positions further away (dash-dotted lines in Fig. 5c) balance out the behavior observed near the tip in such a way that the peak of average lattice temperature (dotted) remains fixed in amplitude for the different pulse durations while being shifted in time when varying Δt (except for the 1 ns case, which is lower because of the heat lost to the environment). However, because of the highly nonlinear dependence of the instantaneous reaction rate on the lattice temperature (through the Arrhenius expression), the dominant number of reactions occur on the tip, leading to the enhanced nonlinearity observed for an integral quantity (over the NP surface) as the number of reactions shown in Fig. 5a. Although the dynamics of the lattice temperature are similar for both reactions, the lattice contribution to O diffusion displays a much smaller peak in Fig. 5b, which is the result of its relatively lower activation energy, causing a sublinear dependence of the instantaneous reaction rate on the lattice

temperature (see Fig. S5). While we underline that reaching the optimal temperature increase at ~1 ps is a quantitative effect specific to the NP material and geometry considered, we argue that the origin of the phenomenon has general validity and it affects measurable quantities (such as the reaction rates). As such, it could be further investigated to enhance photothermal effects upon ultrafast pulsed illumination beyond the steady-state performances.

Conclusions

To conclude, in this work, we have proposed an original model for the ultrafast energy transfer between the hot carriers in plasmonic nanostructures and chemical species adsorbed onto the metal surface to study plasmon photocatalytic events in the ultrashort-pulsed regime of illumination.

By combining in an entirely selfconsistent fashion a rate-equation description of the spatio-temporal dynamics of nonequilibrium carriers with a quantum formalism of the inelastic scattering with molecular adsorbates, our model, referred to as Generalized Extended Two-Temperature Model (GE2TM), allows for quantifying and disentangling the contributions to the reactivity arising from electrons, based on their energy, and the metal lattice temperature. In parallel, by inherently including the temporal resolution on ultrafast timescales, the GE2TM represents the ideal tool to investigate the effects of pulsed light in photocatalysis, which is emerging as an attractive, promising approach to enhance reactivity and selectivity of chemical transformations.

We applied the GE2TM to the representative cases of NO desorption and O diffusion on a Pt(111) surface[57] for a small nanosphere and a larger bowtie nanoantenna. Besides being consistent with previous findings, our analysis enabled us to explain the mechanisms determining the reaction rates typically accessible by experimental means, as well as to predict unexplored regimes for pulsed photocatalysis.

Notably, we observed that, based on the adsorbate energetics, the nonlinearities intrinsic to the thermalized hot carriers (via the Fermi-Dirac distribution) and the lattice (via the Arrhenius formula) can introduce a non-monotonic trend of the reaction rates as a function of pulse duration. The interplay of the ultrafast energy exchange channels available (relaxation, injection, spatial diffusion) is at the origin of enhanced reactivities for specific ultrashort durations of the light pulse.

More generally, thanks to its flexible implementation, the GE2TM can be modified to describe a large set of nanostructured photochemical systems, including different reactions, illumination conditions (wavelength, intensity, pulse duration), as well as arbitrary shape, size, spatial configuration and material. As such, the proposed model could provide accurate, data-comparable predictions and represent a promising step toward the design and optimization of photocatalytic platforms with rationally tailored electronic and thermal properties.

In addition, the model formulation has a rather general validity, making it straightforward to extend the GE2TM to describe the energy transfer from photoexcited electrons in diverse contexts. For instance, by employing different quantum formalisms for the electronic interactions, one could model multielectron processes, the permanent injection of electrons into the adsorbate, or carrier tunneling in a Schottky barrier, beyond the molecular realm. Including more accurate modeling of the molecular dynamics, in principle for both electronically and vibrationally excited states, could also be envisaged to quantitatively investigate the photocatalytic activity for elaborate reactions and larger molecular complexes.

Methods

We implemented Eqs. 1a-1c using the finite element method (FEM) in the commercial software COMSOL Multiphysics. In order to incorporate the energy dependence, we employed the Extra Dimension feature embedded in COMSOL to attach a 1D extra component representing the carrier energy axis to every point in the nanoparticle. First, we calculated the absorption cross section $\sigma_{\mathrm{abs}}(\lambda)$ and the normalized spatial absorption pattern $\rho(\mathbf{r},\lambda)$ across the nanoparticle using a standard electromagnetic simulation in the frequency domain. The corresponding absorption term in Eq. 1a photoexciting nonthermal HCs is then defined as[77, 85]:

$$R_{\mathrm{abs}}(\mathbf{r},t,E) = \frac{1}{A}\delta_{\mathrm{NT}}(E)\left[\rho\left(\mathbf{r},\lambda_{\mathrm{p}}\right)\frac{F_p\sigma_{\mathrm{abs}}(\lambda_{\mathrm{p}})}{V}\right]g(t).$$

Here, F_p is the pulse fluence, V is the nanostructure volume, $g(t) = \sqrt{4\ln 2\,/\pi\Delta t^2}\,\exp\left[-4\ln 2\,(t-t_0)^2\,/\,\Delta t^2\right]$ the Gaussian pulse profile centered at t_0 of duration (full width at half maximum in intensity) Δt, and $\delta_{\mathrm{NT}}(E)$ a double-step-like distribution[73, 77]. The quantity A is a normalization constant defined to ensure energy conservation[74, 76] and expressed as $A = \int_E E\ \mathrm{DOS}(E)\delta_{\mathrm{NT}}(E)\,\mathrm{d}E$. While the energy occupancy distribution of nonthermal electrons is fully determined by $\Delta f_{\mathrm{NT}}(r,t,E)$, the total energy density stored in this fraction of the HC population $N_{\mathrm{NT}}(r,t)$ (in J/cm^3) is defined as the integral over the carrier energies

$$N_{\mathrm{NT}}(\mathbf{r},t) = \int_E E\ \mathrm{DOS}(E)\Delta f_{\mathrm{NT}}(\mathbf{r},t,E)\mathrm{d}E.$$

The energy flowing from the nonthermal to the thermalized HCs is regulated by electron-electron scattering events, whose rate is expressed as the inverse of a collision time τ_{ee} taken from Fermi liquid theory[91]:

$$\tau_{ee}(E) = \tau_0\frac{E_{\mathrm{F}}^2}{(E-E_{\mathrm{F}})^2},$$

where τ_0 is a constant depending on the material[92], for which we set a value of 2 fs in Pt. Similarly, the rate of scattering events between nonthermal HCs and phonons is governed by a characteristic time[73]

$$\tau_{ep} = \tau_{\mathrm{f}}\frac{\hbar\omega_{\mathrm{p}}}{k_{\mathrm{B}}\Theta_{\mathrm{D}}},$$

where Θ_{D} is the Debye temperature of the material and τ_{f} is the quasi-particle free flight time. Values were taken from ref.[57]. Through energy conservation, these rates (τ_{ee}^{-1} and τ_{ep}^{-1}) determine the source terms in Eqs. 1b and 1c as

$$\frac{\partial U_{ex}^{\mathrm{NT}}(\mathbf{r},t)}{\partial t} = \int_E E\ \mathrm{DOS}(E)\Delta f_{\mathrm{NT}}(\mathbf{r},t,E)\frac{1}{\tau_{ex}}\ \mathrm{d}E,$$

where x = e or p refers to energy flowing from nonthermal HCs to either thermalized HCs or the lattice, respectively. The thermal conductivity of the thermalized electrons is defined[93] as $\kappa_{\mathrm{E}} = \kappa_{\mathrm{L}}\frac{\Theta_{\mathrm{E}}}{\Theta_{\mathrm{L}}}$. The electronic heat capacity $C_{\mathrm{E}}(\Theta_{\mathrm{E}})$, thermal electron-phonon coupling constant $G(\Theta_{\mathrm{E}})$, and the metal density of states $\mathrm{DOS}(E)$ are taken from density functional theory calculations available in the literature[94]. In our calculations, we took DOS(E) to be a constant and equal to its value at the Fermi level, which is a valid assumption in that region.

Similarly to Eq. 2, the relaxation channel of thermal electrons due to energy transferred to the adsorbed species is expressed as:

$$Q_{\mathrm{int}}(\mathbf{r},t) = \frac{-1}{\tau_{\mathrm{surf}}}\int_E E\,\mathrm{DOS}(E)\sum_n\left[\Delta f_{\mathrm{T}}(\mathbf{r},t,E+n\hbar\omega_0)P_n(E+n\hbar\omega_0) - \Delta f_{\mathrm{T}}(\mathbf{r},t,E)P_n(E)\right]\mathrm{d}E.$$

Here, following previous reports[57, 65, 66], $P_n(E)$ is defined by the equation

$$P_n(E) = \sum_m P(m\to n\,,E)p_0(m),$$

where $P(m \to n\,, E)$ is the probability that an electron with energy E that scatters off the adsorbate causes a transition from the vibrational state m to state n, and $p_0(m)$ is the probability that the adsorbate initially occupied the vibrational state m at room temperature. The corresponding probability for a reaction with activation barrier E_A to occur is expressed as[57]

$$P_\mathrm{reac}\,(E) = \sum_{n=n_\mathrm{reac}}^{\infty} P_n(E)$$

where n_reac is the integer fulfilling the condition $n_\mathrm{reac}\hbar\omega_0 > E_\mathrm{A}$, $\hbar\omega_0$ being the ground state vibrational spacing defined in the main text (refer to Fig. 1b)

To quantify the energy transferred from plasmonic HCs to the adsorbate, we defined some key quantities. In particular, the instantaneous percentage $P_\mathrm{int}^\mathrm{NT}$ of nonthermal electron energy deposited into the adsorbate (e.g. in Fig. 2e, left axis) was expressed as the integral over electronic energies and nanostructure volume

$$P_\mathrm{int}^\mathrm{NT}(t) \;=\; \frac{1}{U_\mathrm{abs}} \int_\mathrm{NP} \int_E E\;\mathrm{DOS}(E) R_\mathrm{int}(\mathbf{r}, t, E) \mathrm{d}E\;\mathrm{d}V,$$

where $U_\mathrm{abs} = F_\mathrm{p}\sigma_\mathrm{abs}$ is the total absorbed energy. Similarly, for thermalized electrons,

$$P_\mathrm{int}^\mathrm{T}(t) \;=\; \frac{1}{U_\mathrm{abs}} \int_\mathrm{NP} Q_\mathrm{int}(\mathbf{r}, t)\;\mathrm{d}V.$$

The cumulative percentage of energy $U_\mathrm{int}^\mathrm{NT(T)}$ (Fig. 2e, right axis) is then computed as the time integral of the instantaneous one up to the current time t. Finally, the instantaneous rate of reactions induced by nonequilibrium (nonthermal, NT, and thermalized, T) HCs (reported e.g. in Fig 4d, inset) is expressed (in 1/s) as

$$R_\mathrm{reac}^\mathrm{NT(T)}(t) \;=\; \frac{1}{\tau_\mathrm{surf}} \int_\mathrm{NP} \int_E \mathrm{DOS}(E) \Delta f_\mathrm{NT(T)}(\mathbf{r}, t, E) P_\mathrm{reac}(E)\;\mathrm{d}E\;\mathrm{d}V.$$

The cumulative number of reactions $N_\mathrm{reac}^\mathrm{NT(T)}(t)$ (reported e.g. in Fig. 2f) is then computed as the time integral of $R_\mathrm{reac}^\mathrm{NT(T)}(t)$ up to the current time t. To compute instead the rate of reactions induced by the lattice temperature increase $R_\mathrm{reac}^\mathrm{L}(t)$, we employed the Arrhenius law associated with $\Theta_\mathrm{L}(\mathbf{r}, t)$, and integrated it over the nanostructure surface S_NP. To avoid misevaluations of the absolute value of this rate introduced by the pre-factor in the Arrhenius equation, we opted for normalizing $R_\mathrm{reac}^\mathrm{L}(t)$ to its value at room temperature Θ_0. The resulting normalized rate we analyzed (and showed e.g. Fig. 4d) is expressed as:

$$\bar{R}_\mathrm{reac}^\mathrm{L}(t) \;=\; \frac{\int_\mathrm{NP} \exp\left[-\dfrac{E_\mathrm{A}}{k_\mathrm{B}\Theta_\mathrm{L}(\mathbf{r}, t)}\right] \mathrm{d}S}{S_\mathrm{NP} \exp\left[-\dfrac{E_\mathrm{A}}{k_\mathrm{B}\Theta_0}\right]} - 1.$$

Acknowledgements

A.S. and G.D.V acknowledge financial support by the European Union's NextGenerationEU Programme with the I-PHOQS Infrastructure [IR0000016, ID D2B8D520, CUP B53C22001750006] "Integrated infrastructure initiative in Photonic and Quantum Sciences", and from the METAFAST project that received funding from the European Union Horizon 2020 Research and Innovation program under Grant Agreement No. 899673. This work reflects only the author's view, and the European Commission is not responsible for any use that may be made of the information it contains. G.D.V. acknowledges the support from the HOTMETA project under the PRIN 2022 MUR program funded by the European Union – Next Generation EU - "PNRR - M4C2, investimento 1.1 - "Fondo PRIN 2022" - HOT-carrier METasurfaces for Advanced photonics (HOTMETA), contract no. 2022LENW33 - CUP: D53D2300229 0006". P.N.

acknowledges support from the Robert A. Welch foundation under grant C-1222 and the Air Force Office of Scientific Research via the Department of Defense Multidisciplinary University Research Initiative under AFOSR Award No. FA9550-15-1-0022.

References

1. Smith, C.; Hill, A. K.; Torrente-Murciano, L., Current and future role of Haber–Bosch ammonia in a carbon-free energy landscape. *Energy & Environmental Science* **2020,** *13* (2), 331-344.
2. IEA, World Energy Investment. *IEA, Paris* **2023,** https://www.iea.org/reports/world-energy-investment-2023.
3. Christopher, P.; Xin, H.; Linic, S., Visible-light-enhanced catalytic oxidation reactions on plasmonic silver nanostructures. *Nature Chemistry* **2011,** *3* (6), 467-472.
4. Song, C.; Wang, Z.; Yin, Z.; Xiao, D.; Ma, D., Principles and applications of photothermal catalysis. *Chem Catalysis* **2022,** *2* (1), 52-83.
5. Linic, S.; Aslam, U.; Boerigter, C.; Morabito, M., Photochemical transformations on plasmonic metal nanoparticles. *Nature Materials* **2015,** *14* (6), 567-576.
6. Li, S.; Miao, P.; Zhang, Y.; Wu, J.; Zhang, B.; Du, Y.; Han, X.; Sun, J.; Xu, P., Recent Advances in Plasmonic Nanostructures for Enhanced Photocatalysis and Electrocatalysis. *Advanced Materials* **2021,** *33* (6), 2000086.
7. Maier, S. A., *Plasmonics: Fundamentals and Applications*. 1st ed. 2007. ed.; Springer US: New York, NY, 2007.
8. Schuller, J. A.; Barnard, E. S.; Cai, W.; Jun, Y. C.; White, J. S.; Brongersma, M. L., Plasmonics for extreme light concentration and manipulation. *Nature Materials* **2010,** *9* (3), 193-204.
9. Brongersma, M. L.; Halas, N. J.; Nordlander, P., Plasmon-induced hot carrier science and technology. *Nature Nanotechnology* **2015,** *10* (1), 25-34.
10. Besteiro, L. V.; Yu, P.; Wang, Z.; Holleitner, A. W.; Hartland, G. V.; Wiederrecht, G. P.; Govorov, A. O., The fast and the furious: Ultrafast hot electrons in plasmonic metastructures. Size and structure matter. *Nano Today* **2019,** *27*, 120-145.
11. Govorov, A. O.; Zhang, H.; Gun'ko, Y. K., Theory of Photoinjection of Hot Plasmonic Carriers from Metal Nanostructures into Semiconductors and Surface Molecules. *The Journal of Physical Chemistry C* **2013,** *117* (32), 16616-16631.
12. Kale, M. J.; Avanesian, T.; Christopher, P., Direct Photocatalysis by Plasmonic Nanostructures. *ACS Catalysis* **2014,** *4* (1), 116-128.
13. Zhang, Y.; He, S.; Guo, W.; Hu, Y.; Huang, J.; Mulcahy, J. R.; Wei, W. D., Surface-Plasmon-Driven Hot Electron Photochemistry. *Chemical Reviews* **2018,** *118* (6), 2927-2954.
14. Lindstrom, C. D.; Zhu, X. Y., Photoinduced Electron Transfer at Molecule−Metal Interfaces. *Chemical Reviews* **2006,** *106* (10), 4281-4300.
15. Baffou, G.; Quidant, R., Thermo-plasmonics: using metallic nanostructures as nano-sources of heat. *Laser & Photonics Reviews* **2013,** *7* (2), 171-187.
16. Baffou, G.; Quidant, R., Nanoplasmonics for chemistry. *Chemical Society Reviews* **2014,** *43* (11), 3898-3907.
17. Cortés, E.; Besteiro, L. V.; Alabastri, A.; Baldi, A.; Tagliabue, G.; Demetriadou, A.; Narang, P., Challenges in Plasmonic Catalysis. *ACS Nano* **2020,** *14* (12), 16202-16219.
18. Robatjazi, H.; Yuan, L.; Yuan, Y.; Halas, N. J., Heterogeneous Plasmonic Photocatalysis: Light-Driven Chemical Reactions Introduce a New Approach to Industrially-Relevant Chemistry. In *Emerging Trends in Chemical Applications of Lasers*, American Chemical Society: 2021; Vol. 1398, pp 363-387.
19. Mukherjee, S.; Libisch, F.; Large, N.; Neumann, O.; Brown, L. V.; Cheng, J.; Lassiter, J. B.; Carter, E. A.; Nordlander, P.; Halas, N. J., Hot Electrons Do the Impossible: Plasmon-Induced Dissociation of H2 on Au. *Nano Letters* **2013,** *13* (1), 240-247.
20. Boerigter, C.; Campana, R.; Morabito, M.; Linic, S., Evidence and implications of direct charge excitation as the dominant mechanism in plasmon-mediated photocatalysis. *Nature Communications* **2016,** *7* (1), 10545.
21. Li, H.; Qin, F.; Yang, Z.; Cui, X.; Wang, J.; Zhang, L., New Reaction Pathway Induced by Plasmon for Selective Benzyl Alcohol Oxidation on BiOCl Possessing Oxygen Vacancies. *Journal of the American Chemical Society* **2017,** *139* (9), 3513-3521.

22. Zhang, X.; Li, X.; Zhang, D.; Su, N. Q.; Yang, W.; Everitt, H. O.; Liu, J., Product selectivity in plasmonic photocatalysis for carbon dioxide hydrogenation. *Nature Communications* **2017,** *8* (1), 14542.
23. Sytwu, K.; Vadai, M.; Hayee, F.; Angell, D. K.; Dai, A.; Dixon, J.; Dionne, J. A., Driving energetically unfavorable dehydrogenation dynamics with plasmonics. *Science* **2021,** *371* (6526), 280-283.
24. Marimuthu, A.; Zhang, J.; Linic, S., Tuning Selectivity in Propylene Epoxidation by Plasmon Mediated Photo-Switching of Cu Oxidation State. *Science* **2013,** *339* (6127), 1590-1593.
25. Robatjazi, H.; Zhao, H.; Swearer, D. F.; Hogan, N. J.; Zhou, L.; Alabastri, A.; McClain, M. J.; Nordlander, P.; Halas, N. J., Plasmon-induced selective carbon dioxide conversion on earth-abundant aluminum-cuprous oxide antenna-reactor nanoparticles. *Nature Communications* **2017,** *8* (1), 27.
26. Zhou, L.; Martirez, J. M. P.; Finzel, J.; Zhang, C.; Swearer, D. F.; Tian, S.; Robatjazi, H.; Lou, M.; Dong, L.; Henderson, L.; Christopher, P.; Carter, E. A.; Nordlander, P.; Halas, N. J., Light-driven methane dry reforming with single atomic site antenna-reactor plasmonic photocatalysts. *Nature Energy* **2020,** *5* (1), 61-70.
27. Yuan, Y.; Zhou, L.; Robatjazi, H.; Bao, J. L.; Zhou, J.; Bayles, A.; Yuan, L.; Lou, M.; Lou, M.; Khatiwada, S.; Carter, E. A.; Nordlander, P.; Halas, N. J., Earth-abundant photocatalyst for H2 generation from NH3 with light-emitting diode illumination. *Science* **2022,** *378* (6622), 889-893.
28. Christopher, P.; Xin, H.; Marimuthu, A.; Linic, S., Singular characteristics and unique chemical bond activation mechanisms of photocatalytic reactions on plasmonic nanostructures. *Nature Materials* **2012,** *11* (12), 1044-1050.
29. Kim, Y.; Dumett Torres, D.; Jain, P. K., Activation Energies of Plasmonic Catalysts. *Nano Letters* **2016,** *16* (5), 3399-3407.
30. Zhou, L.; Swearer, D. F.; Zhang, C.; Robatjazi, H.; Zhao, H.; Henderson, L.; Dong, L.; Christopher, P.; Carter, E. A.; Nordlander, P.; Halas, N. J., Quantifying hot carrier and thermal contributions in plasmonic photocatalysis. *Science* **2018,** *362* (6410), 69-72.
31. Robatjazi, H.; Bao, J. L.; Zhang, M.; Zhou, L.; Christopher, P.; Carter, E. A.; Nordlander, P.; Halas, N. J., Plasmon-driven carbon–fluorine (C(sp3)–F) bond activation with mechanistic insights into hot-carrier-mediated pathways. *Nature Catalysis* **2020,** *3* (7), 564-573.
32. Aizpurua, J.; Ashfold, M.; Baletto, F.; Baumberg, J.; Christopher, P.; Cortés, E.; de Nijs, B.; Diaz Fernandez, Y.; Gargiulo, J.; Gawinkowski, S.; Halas, N.; Hamans, R.; Jankiewicz, B.; Khurgin, J.; Kumar, P. V.; Liu, J.; Maier, S.; Maurer, R. J.; Mount, A.; Mueller, N. S.; Oulton, R.; Parente, M.; Park, J. Y.; Polanyi, J.; Quiroz, J.; Rejman, S.; Schlücker, S.; Schultz, Z.; Sivan, Y.; Tagliabue, G.; Thangamuthu, M.; Torrente-Murciano, L.; Xiao, X.; Zayats, A.; Zhan, C., Dynamics of hot electron generation in metallic nanostructures: general discussion. *Faraday Discussions* **2019,** *214* (0), 123-146.
33. Liu, J. G.; Zhang, H.; Link, S.; Nordlander, P., Relaxation of Plasmon-Induced Hot Carriers. *ACS Photonics* **2018,** *5* (7), 2584-2595.
34. Sun, C. K.; Vallée, F.; Acioli, L. H.; Ippen, E. P.; Fujimoto, J. G., Femtosecond-tunable measurement of electron thermalization in gold. *Physical Review B* **1994,** *50* (20), 15337-15348.
35. Tagliabue, G.; DuChene, J. S.; Abdellah, M.; Habib, A.; Gosztola, D. J.; Hattori, Y.; Cheng, W.-H.; Zheng, K.; Canton, S. E.; Sundararaman, R.; Sá, J.; Atwater, H. A., Ultrafast hot-hole injection modifies hot-electron dynamics in Au/p-GaN heterostructures. *Nature Materials* **2020,** *19* (12), 1312-1318.
36. Kim, K. H.; Watanabe, K.; Mulugeta, D.; Freund, H.-J.; Menzel, D., Enhanced Photoinduced Desorption from Metal Nanoparticles by Photoexcitation of Confined Hot Electrons Using Femtosecond Laser Pulses. *Physical Review Letters* **2011,** *107* (4), 047401.
37. Stépán, K.; Güdde, J.; Höfer, U., Time-Resolved Measurement of Surface Diffusion Induced by Femtosecond Laser Pulses. *Physical Review Letters* **2005,** *94* (23), 236103.
38. Qi, J.; Resasco, J.; Robatjazi, H.; Alvarez, I. B.; Abdelrahman, O.; Dauenhauer, P.; Christopher, P., Dynamic Control of Elementary Step Energetics via Pulsed Illumination Enhances Photocatalysis on Metal Nanoparticles. *ACS Energy Letters* **2020,** *5* (11), 3518-3525.
39. Wang, Y.; Wang, Y.; Aravind, I.; Cai, Z.; Shen, L.; Zhang, B.; Wang, B.; Chen, J.; Zhao, B.; Shi, H.; Dawlaty, J. M.; Cronin, S. B., In Situ Investigation of Ultrafast Dynamics of Hot Electron-Driven

Photocatalysis in Plasmon-Resonant Grating Structures. *Journal of the American Chemical Society* **2022,** *144* (8), 3517-3526.
40. Baldi, A.; Askes, S. H. C., Pulsed Photothermal Heterogeneous Catalysis. *ACS Catalysis* **2023,** *13* (5), 3419-3432.
41. Wang, C.; Ranasingha, O.; Natesakhawat, S.; Ohodnicki, P. R.; Andio, M.; Lewis, J. P.; Matranga, C., Visible light plasmonic heating of Au–ZnO for the catalytic reduction of CO2. *Nanoscale* **2013,** *5* (15), 6968-6974.
42. Dong, Q.; Yao, Y.; Cheng, S.; Alexopoulos, K.; Gao, J.; Srinivas, S.; Wang, Y.; Pei, Y.; Zheng, C.; Brozena, A. H.; Zhao, H.; Wang, X.; Toraman, H. E.; Yang, B.; Kevrekidis, I. G.; Ju, Y.; Vlachos, D. G.; Liu, D.; Hu, L., Programmable heating and quenching for efficient thermochemical synthesis. *Nature* **2022,** *605* (7910), 470-476.
43. Sadle, E. S.; Kostin, M. D., INCREASED PRODUCTION RATE OF AMMONIA BY PULSED HEATING. *Chemical Engineering Communications* **1984,** *26*, 265-268.
44. Bailey, J. E., PERIODIC OPERATION OF CHEMICAL REACTORS: A REVIEW. *Chemical Engineering Communications* **1974,** *1* (3), 111-124.
45. Manjavacas, A.; Liu, J. G.; Kulkarni, V.; Nordlander, P., Plasmon-Induced Hot Carriers in Metallic Nanoparticles. *ACS Nano* **2014,** *8* (8), 7630-7638.
46. Narang, P.; Sundararaman, R.; Atwater, H. A., Plasmonic hot carrier dynamics in solid-state and chemical systems for energy conversion. *Nanophotonics* **2016,** *5* (1), 96-111.
47. João, S. M.; Jin, H.; Lischner, J. C., Atomistic Theory of Hot-Carrier Relaxation in Large Plasmonic Nanoparticles. *The Journal of Physical Chemistry C* **2023,** *127* (48), 23296-23302.
48. Sundararaman, R.; Narang, P.; Jermyn, A. S.; Goddard Iii, W. A.; Atwater, H. A., Theoretical predictions for hot-carrier generation from surface plasmon decay. *Nature Communications* **2014,** *5* (1), 5788.
49. Vanzan, M.; Gil, G.; Castaldo, D.; Nordlander, P.; Corni, S., Energy Transfer to Molecular Adsorbates by Transient Hot Electron Spillover. *Nano Letters* **2023,** *23* (7), 2719-2725.
50. Martirez, J. M. P.; Bao, J. L.; Carter, E. A., First-Principles Insights into Plasmon-Induced Catalysis. *Annual Review of Physical Chemistry* **2021,** *72* (1), 99-119.
51. Spata, V. A.; Carter, E. A., Mechanistic Insights into Photocatalyzed Hydrogen Desorption from Palladium Surfaces Assisted by Localized Surface Plasmon Resonances. *ACS Nano* **2018,** *12* (4), 3512-3522.
52. Schirato, A.; Maiuri, M.; Cerullo, G.; Della Valle, G., Ultrafast hot electron dynamics in plasmonic nanostructures: experiments, modelling, design. **2023,** *12* (1), 1-28.
53. Brown, A. M.; Sundararaman, R.; Narang, P.; Schwartzberg, A. M.; Goddard, W. A.; Atwater, H. A., Experimental and Ab Initio Ultrafast Carrier Dynamics in Plasmonic Nanoparticles. *Physical Review Letters* **2017,** *118* (8), 087401.
54. Nahm, T. U.; Gomer, R., The adsorption of methane on W(110). *Surface Science* **1997,** *389* (1), 177-187.
55. Wagstaffe, M.; Wenthaus, L.; Dominguez-Castro, A.; Chung, S.; Lana Semione, G. D.; Palutke, S.; Mercurio, G.; Dziarzhytski, S.; Redlin, H.; Klemke, N.; Yang, Y.; Frauenheim, T.; Dominguez, A.; Kärtner, F.; Rubio, A.; Wurth, W.; Stierle, A.; Noei, H., Ultrafast Real-Time Dynamics of CO Oxidation over an Oxide Photocatalyst. *ACS Catalysis* **2020,** *10* (22), 13650-13658.
56. Nilsson, A.; LaRue, J.; Öberg, H.; Ogasawara, H.; Dell'Angela, M.; Beye, M.; Öström, H.; Gladh, J.; Nørskov, J. K.; Wurth, W.; Abild-Pedersen, F.; Pettersson, L. G. M., Catalysis in real time using X-ray lasers. *Chemical Physics Letters* **2017,** *675*, 145-173.
57. Avanesian, T.; Christopher, P., Adsorbate Specificity in Hot Electron Driven Photochemistry on Catalytic Metal Surfaces. *The Journal of Physical Chemistry C* **2014,** *118* (48), 28017-28031.
58. Kong, X.-T.; Wang, Z.; Govorov, A. O., Plasmonic Nanostars with Hot Spots for Efficient Generation of Hot Electrons under Solar Illumination. *Advanced Optical Materials* **2017,** *5* (15).

59. Lyu, P.-T.; Yin, L.-X.; Shen, Y.-T.; Gao, Z.; Chen, H.-Y.; Xu, J.-J.; Kang, B., Plasmonic Cavity-Catalysis by Standing Hot Carrier Waves. *Journal of the American Chemical Society* **2023,** *145* (34), 18912-18919.
60. Gargiulo, J.; Berté, R.; Li, Y.; Maier, S. A.; Cortés, E., From Optical to Chemical Hot Spots in Plasmonics. *Accounts of Chemical Research* **2019,** *52* (9), 2525-2535.
61. Swearer, D. F.; Zhao, H.; Zhou, L.; Zhang, C.; Robatjazi, H.; Martirez, J. M. P.; Krauter, C. M.; Yazdi, S.; McClain, M. J.; Ringe, E.; Carter, E. A.; Nordlander, P.; Halas, N. J., Heterometallic antenna−reactor complexes for photocatalysis. *Proceedings of the National Academy of Sciences* **2016,** *113* (32), 8916-8920.
62. Yuan, L.; Zhou, J.; Zhang, M.; Wen, X.; Martirez, J. M. P.; Robatjazi, H.; Zhou, L.; Carter, E. A.; Nordlander, P.; Halas, N. J., Plasmonic Photocatalysis with Chemically and Spatially Specific Antenna–Dual Reactor Complexes. *ACS Nano* **2022,** *16* (10), 17365-17375.
63. Gadzuk, J. W., Resonance-assisted, hot-electron-induced desorption. *Surface Science* **1995,** *342* (1), 345-358.
64. Gadzuk, J. W., Inelastic resonance scattering, tunneling, and desorption. *Physical Review B* **1991,** *44* (24), 13466-13477.
65. Olsen, T.; Gavnholt, J.; Schiøtz, J., Hot-electron-mediated desorption rates calculated from excited-state potential energy surfaces. *Physical Review B* **2009,** *79* (3), 035403.
66. Kale, M. J.; Avanesian, T.; Xin, H.; Yan, J.; Christopher, P., Controlling Catalytic Selectivity on Metal Nanoparticles by Direct Photoexcitation of Adsorbate–Metal Bonds. *Nano Letters* **2014,** *14* (9), 5405-5412.
67. Besteiro, L. V.; Kong, X.-T.; Wang, Z.; Hartland, G.; Govorov, A. O., Understanding Hot-Electron Generation and Plasmon Relaxation in Metal Nanocrystals: Quantum and Classical Mechanisms. *ACS Photonics* **2017,** *4* (11), 2759-2781.
68. Gadzuk, J. W.; Richter, L. J.; Buntin, S. A.; King, D. S.; Cavanagh, R. R., Laser-excited hot-electron induced desorption: A theoretical model applied to NO/Pt(111). *Surface Science* **1990,** *235* (2), 317-333.
69. Gavnholt, J.; Rubio, A.; Olsen, T.; Thygesen, K. S.; Schiøtz, J., Hot-electron-assisted femtochemistry at surfaces: A time-dependent density functional theory approach. *Physical Review B* **2009,** *79* (19), 195405.
70. Linic, S.; Christopher, P.; Ingram, D. B., Plasmonic-metal nanostructures for efficient conversion of solar to chemical energy. *Nature Materials* **2011,** *10* (12), 911-921.
71. Bonn, M.; Funk, S.; Hess, C.; Denzler, D. N.; Stampfl, C.; Scheffler, M.; Wolf, M.; Ertl, G., Phonon- Versus Electron-Mediated Desorption and Oxidation of CO on Ru(0001). *Science* **1999,** *285* (5430), 1042-1045.
72. Lisowski, M.; Loukakos, P. A.; Bovensiepen, U.; Stähler, J.; Gahl, C.; Wolf, M., Ultra-fast dynamics of electron thermalization, cooling and transport effects in Ru(001). *Applied Physics A* **2004,** *78* (2), 165-176.
73. Carpene, E., Ultrafast laser irradiation of metals: Beyond the two-temperature model. *Physical Review B* **2006,** *74* (2), 024301.
74. Della Valle, G.; Conforti, M.; Longhi, S.; Cerullo, G.; Brida, D., Real-time optical mapping of the dynamics of nonthermal electrons in thin gold films. *Physical Review B* **2012,** *86* (15), 155139.
75. O'Keeffe, P.; Catone, D.; Di Mario, L.; Toschi, F.; Magnozzi, M.; Bisio, F.; Alabastri, A.; Proietti Zaccaria, R.; Toma, A.; Della Valle, G.; Paladini, A., Disentangling the Temporal Dynamics of Nonthermal Electrons in Photoexcited Gold Nanostructures. *Laser & Photonics Reviews* **2021,** *15* (6), 2100017.
76. Zavelani-Rossi, M.; Polli, D.; Kochtcheev, S.; Baudrion, A.-L.; Béal, J.; Kumar, V.; Molotokaite, E.; Marangoni, M.; Longhi, S.; Cerullo, G.; Adam, P.-M.; Della Valle, G., Transient Optical Response of a Single Gold Nanoantenna: The Role of Plasmon Detuning. *ACS Photonics* **2015,** *2* (4), 521-529.

77. Schirato, A.; Maiuri, M.; Toma, A.; Fugattini, S.; Proietti Zaccaria, R.; Laporta, P.; Nordlander, P.; Cerullo, G.; Alabastri, A.; Della Valle, G., Transient optical symmetry breaking for ultrafast broadband dichroism in plasmonic metasurfaces. *Nature Photonics* **2020,** *14* (12), 723-727.
78. Coronado, E. A.; Schatz, G. C., Surface plasmon broadening for arbitrary shape nanoparticles: A geometrical probability approach. *The Journal of Chemical Physics* **2003,** *119* (7), 3926-3934.
79. Menzel, D.; Gomer, R., Desorption from Metal Surfaces by Low-Energy Electrons. *The Journal of Chemical Physics* **2004,** *41* (11), 3311-3328.
80. Redhead, P. A., INTERACTION OF SLOW ELECTRONS WITH CHEMISORBED OXYGEN. *Canadian Journal of Physics* **1964,** *42* (5), 886-905.
81. Yamanaka, T.; Hellman, A.; Gao, S.; Ho, W., State-resolved femtosecond two-pulse correlation measurements of NO photodesorption from Pt(111). *Surface Science* **2002,** *514* (1), 404-408.
82. Kalz, K. F.; Kraehnert, R.; Dvoyashkin, M.; Dittmeyer, R.; Gläser, R.; Krewer, U.; Reuter, K.; Grunwaldt, J.-D., Future Challenges in Heterogeneous Catalysis: Understanding Catalysts under Dynamic Reaction Conditions. *ChemCatChem* **2017,** *9* (1), 17-29.
83. Giugni, A.; Torre, B.; Toma, A.; Francardi, M.; Malerba, M.; Alabastri, A.; Proietti Zaccaria, R.; Stockman, M. I.; Di Fabrizio, E., Hot-electron nanoscopy using adiabatic compression of surface plasmons. *Nature Nanotechnology* **2013,** *8* (11), 845-852.
84. Askes, S. H. C.; Garnett, E. C., Ultrafast Thermal Imprinting of Plasmonic Hotspots. *Advanced Materials* **2021,** *33* (49), 2105192.
85. Schirato, A.; Crotti, G.; Proietti Zaccaria, R.; Alabastri, A.; Della Valle, G., Hot carrier spatio-temporal inhomogeneities in ultrafast nanophotonics. *New Journal of Physics* **2022,** *24* (4), 045001.
86. Cunha, J.; Guo, T.-L.; Koya, A. N.; Toma, A.; Prato, M.; Della Valle, G.; Alabastri, A.; Proietti Zaccaria, R., Photoinduced Temperature Gradients in Sub-Wavelength Plasmonic Structures: The Thermoplasmonics of Nanocones. *Advanced Optical Materials* **2020,** *8* (18), 2000568.
87. Cortés, E.; Xie, W.; Cambiasso, J.; Jermyn, A. S.; Sundararaman, R.; Narang, P.; Schlücker, S.; Maier, S. A., Plasmonic hot electron transport drives nano-localized chemistry. *Nature Communications* **2017,** *8* (1), 14880.
88. Misewich, J. A.; Heinz, T. F.; Newns, D. M., Desorption induced by multiple electronic transitions. *Physical Review Letters* **1992,** *68* (25), 3737-3740.
89. Gadzuk, J. W., Hot-electron femtochemistry at surfaces: on the role of multiple electron processes in desorption. *Chemical Physics* **2000,** *251* (1), 87-97.
90. Olsen, T.; Schiøtz, J., Origin of Power Laws for Reactions at Metal Surfaces Mediated by Hot Electrons. *Physical Review Letters* **2009,** *103* (23), 238301.
91. Pines, D., *Theory of quantum liquids*. CRC Press: London, England, 2019.
92. Fann, W. S.; Storz, R.; Tom, H. W. K.; Bokor, J., Electron thermalization in gold. *Physical Review B* **1992,** *46* (20), 13592-13595.
93. Kanavin, A. P.; Smetanin, I. V.; Isakov, V. A.; Afanasiev, Y. V.; Chichkov, B. N.; Wellegehausen, B.; Nolte, S.; Momma, C.; Tünnermann, A., Heat transport in metals irradiated by ultrashort laser pulses. *Physical Review B* **1998,** *57* (23), 14698-14703.
94. Lin, Z.; Zhigilei, L. V.; Celli, V., Electron-phonon coupling and electron heat capacity of metals under conditions of strong electron-phonon nonequilibrium. *Physical Review B* **2008,** *77* (7), 075133.